Projection Reconstruction MR Imaging Using FOCUSS

Jong Chul Ye,[1]* Sungho Tak,[1] Yeji Han,[2] and Hyun Wook Park[2]

The focal underdetermined system solver (FOCUSS) was originally designed to obtain sparse solutions by successively solving quadratic optimization problems. This article adapts FOCUSS for a projection reconstruction MR imaging problem to obtain high resolution reconstructions from angular undersampled radial *k*-space data. We show that FOCUSS is effective for projection reconstruction MRI, since medical images are usually sparse in some sense and the center region of the undersampled radial *k*-space samples still provides a low resolution, yet meaningful, image essential for the convergence of FOCUSS. The new algorithm is successfully applied for synthetic data as well as in vivo brain imaging obtained by under-sampled radial spin echo sequence. Magn Reson Med 57:764–775, 2007.

Key words: projection reconstruction; sparsity; angular undersampling; FOCUSS; compressed sensing

Projection reconstruction (PR) with radial *k*-space trajectory was the first MRI *k*-space trajectory in MR history (1). However, cartesian *k*-space trajectory has replaced PR, mainly because of artifacts of PR that are related to B_0 inhomogeneity and to gradient nonlinearity (2). However, recent advances in MR hardware technology have overcome problems related to B_0 inhomogeneity and gradient nonlinearity, and interest in PR has thus been revived. PR has many advantages over the conventional cartesian *k*-space trajectory (3). Since no phase-encoding gradient is used, PR has a shorter minimum TE, which has made PR particularly desirable for imaging very short T_2 nuclei (3–5). Another advantage of PR is its robustness to the motion artifacts from flow or respiration. One important example is the reduction of motion artifacts in a diffusion-weighted MRI (6,7). Furthermore, the aliasing artifacts from radial under-sampling usually appear as streaks, which are visually less distracting than the wrap-around artifacts obtained with cartesian under-sampling.

One of the disadvantages of PR is the increased scan time involved if the Nyquist sampling criterion needs to be satisfied. More specifically, the number of radial lines N_s required to satisfy the Nyquist criterion is given by (3):

$$N_s \geq \pi k_{\max} L, \qquad [1]$$

where L is the field-of-view (FOV), and $k_{\max}$ is the maximum *k*-space radius. Usually, the number of radial lines acquired by PR is about 57% larger than the number of *k*-space lines acquired on a cartesian grid, which results in the increased scan time (3). If streak aliasing artifacts can be tolerated in an application, the scan time can be reduced by using angular undersampling. One such undersampled PR application is contrast-enhanced vascular imaging (8). Because of the properties of PR, if the contrast enhanced vessels are located at the center of the FOV, the undersampling aliasing artifacts appear as streaks near the periphery of the FOV and usually do not interfere with vessels located at the center of FOV. Hence, this application of PR for angiography has been a success (8).

Rather than tolerating the angular aliasing artifacts, however, the main goal of our research is to develop a novel reconstruction algorithm with minimal angular aliasing. The bases of such a novel algorithm are the following two observations: (a) most medical imaging is sparse in some sense, and (b) the under-sampled PR still provides a meaningful low resolution image.

Recently, there has been great interest in super-resolution MR image reconstruction techniques from highly undersampled *k*-space data, including k-t SPARSE (9,10), and HYPR (11). The advantage of using the highly undersampled *k*-space data is fast acquisition, which improves the temporal resolution. Mathematically, the reconstruction problem from sparse *k*-space samples is an ill-posed inverse problem with infinitely many solutions; therefore, some kind of regularization or constraint is necessary to obtain a unique and stable reconstruction. Sparsity is a very promising constraint for such ill-posed inverse problems, because sparse images are quite often encountered in practise, and the sparsity constraint does not usually sacrifice the image resolution. For example, in MR angiography problems, the support of the vascular structures only assumes a small portion of the total field of view. Even for other imaging applications, such as brain or cardiac imaging, an image can be sparsified under some transformation, such as wavelet transform or temporal Fourier transform. Assuming a given image can be sparsified, the recent theory of so-called "compressed sensing" (12,13) in the signal processing community shows that perfect reconstruction is possible even from samples markedly smaller than the Nyquist sampling limit. Even for images not completely sparse, the compressed sensing theory tells us that significant features of images can be still obtained. Furthermore, the basis pursuit, matching pursuit methods, or the convex L_1 optimization method can be used to obtain sparse solutions (12,13). In MR imaging, k-t SPARSE successively employed the compressed sensing theory for cardiac imaging applications by transforming the time varying image using a wavelet transform along the spatial direction and a Fourier transform along the temporal direction (9). The compressed sensing concept has been also used for the MR angiography problem (10).

The main contribution of this article is to demonstrate that a new type of sparse reconstruction algorithm called

[1]Department of Biosystems, Korea Advanced Institute of Science & Technology, Daejon 305-701, Korea

[2]Department of Electrical and Computer Engineering, Korea Advanced Institute of Science & Technology, Daejon 305-701, Korea

*Correspondence to: Jong Chul Ye, Assistant Professor, Department of Biosystems, Korea Advanced Institute of Science & Technology, 373-1 Guseong-dong Yuseong-gu, Daejon 305-701, Korea. E-mail: jong.ye@kaist.ac.kr

Received 1 August 2006; revised 29 December 2006; accepted 3 January 2007.

DOI 10.1002/mrm.21202

Published online in Wiley InterScience (www.interscience.wiley.com).

the focal underdetermined system solver (FOCUSS) (14–16) is suitable for projection reconstruction MR imaging. FOCUSS was originally designed for electroencephalogram (EEG) and magnetoencephalography (MEG) source localization problems by obtaining sparse solutions from successive quadratic optimization problems (14,15). More specifically, FOCUSS starts from a low resolution estimate of the sparse signal, which is pruned to a sparse signal representation. The pruning process is implemented by scaling the entries of the current solution by the function of the solutions of previous iterations. Therefore, one of the important requirements of FOCUSS is the existence of an initial estimate with reasonably low resolution to provide the necessary extra constraint to resolve the nonuniqueness of the problem.

FOCUSS is a nice fit to the projection reconstruction MRI in many aspects. First, in the MR imaging problem from radial under-sampled data, the conventional back-projection of the down-sampled data provides the necessary low-resolution initial estimate, which is essential for FOCUSS. This is because the oversampled center region provides a low resolution, yet meaningful, image. Second, FOCUSS incorporates the sparseness of the image as a soft-constraint, whereas the conventional basis pursuit or orthogonal matching pursuit imposes the constraint as a hard constraint. The hard sparseness constraint may be unsuitable for medical imaging applications, since the abrupt changes of the image values depending on the support introduce visually annoying high frequency artifacts. The reconstruction image using FOCUSS, however, does not have these characteristics, since the nonzero image values are gradually suppressed. Third, even if the image is not sparse in the strict sense, FOCUSS tends to suppress the reconstruction noise because aliasing artifacts and noises are usually isolated; thus, they can be easily removed during the pruning process of FOCUSS. Finally, FOCUSS can be very easily implemented in a computationally efficient manner using successive quadratic optimization. This is a quite significant advantage over computationally expensive sparse optimization algorithms, such as basis pursuit or matching pursuit (12,13). Indeed, because of the special structure of the projection reconstruction MRI, the FOCUSS algorithm can be efficiently implemented using an iterative application of back-projection and reprojection. Hence, the fast projection/back-projection algorithm (17,18) can be used to minimize the computational burden. Because of these advantages of FOCUSS in projection reconstruction MRI, we term the new algorithm the projection reconstruction focal underdetermined system solver (PR-FOCUSS). Experimental results using synthetic and in vivo data demonstrate very quick convergence of our algorithm to accurate solutions even from highly sparse k-space samples.

SPARSE RECONSTRUCTION USING FOCUSS

Notation

Throughout the article, the matrix is represented by a bold capital letter (e.g., $\mathbf{W}$), whereas a bold lowercase letter (e.g., $\mathbf{x}$) represents the vector. The (i, j)-th elements of $\mathbf{W}$ are represented by $W_{i,j}$, and the ith elements of $\mathbf{x}$ are x_i. In the lth FOCUSS iteration, the updates of a vector $\mathbf{x}$ and a matrix $\mathbf{W}$ are represented by $\mathbf{x}_l$ and $\mathbf{W}_l$, respectively. Then, the ith elements of the vector $\mathbf{x}_l$ are represented by $x_{l;i}$. As will be shown later, within the lth FOCUSS step, there exists conjugate gradient steps. The nth update for $\mathbf{x}_l$ from the conjugate gradient iteration is then represented by $\mathbf{x}_l^{(n)}$.

Review of FOCUSS

FOCUSS is an algorithm designed to obtain sparse solutions to underdetermined linear inverse problem given by

$$\mathbf{y} = \mathbf{A}\mathbf{x}, \qquad [2]$$

where $\mathbf{y} \in \mathbb{C}^K$, $\mathbf{x} \in \mathbb{C}^N$, $\mathbf{A}$ is a $K \times N$ matrix, and $N \gg K$ (15,16). There exist infinitely many solutions to Eq. [2], and the minimum norm solution is the most widely used for Eq. [2]. This minimum norm solution is uniquely computed by solving the following minimization problem:

$$\min \|\mathbf{x}\|_2^2, \quad \text{s.t. } \mathbf{A}\mathbf{x} = \mathbf{y}, \qquad [3]$$

where $\|\cdot\|_2$ denotes the L_2 norm. Then, the solution can be represented in a closed form:

$$\mathbf{x} = \mathbf{A}^\dagger \mathbf{y}, \qquad [4]$$

where $\mathbf{A}^\dagger = \mathbf{A}^H(\mathbf{A}\mathbf{A}^H)^{-1}$ denotes the pseudo-inverse. The minimum norm solution has the tendency to spread the energy rather than obtaining sparse solution (15,16).

To derive FOCUSS, let us consider the following optimization problem:

$$\text{find } \mathbf{x} = \mathbf{W}\mathbf{q}, \qquad [5]$$

where $\mathbf{x}$ is the unknown image, $\mathbf{W}$ is a weighting matrix, and $\mathbf{q}$ is computed from the following constrained minimization problem:

$$\min \|\mathbf{q}\|_2^2, \text{ s.t. } \mathbf{A}\mathbf{W}\mathbf{q} = \mathbf{y}. \qquad [6]$$

Note the difference between the minimization problems of Eqs. [3] and [6]. The difference is the inclusion of the weighting matrix $\mathbf{W}$ right after the $\mathbf{A}$ matrix. Now, the optimal solution is given by

$$\begin{aligned} \mathbf{q} &= (\mathbf{A}\mathbf{W})^\dagger \mathbf{y}, \\ \mathbf{x} &= \mathbf{W}\mathbf{q} = \mathbf{W}(\mathbf{A}\mathbf{W})^\dagger \mathbf{y}. \end{aligned} \qquad [7]$$

This is the basic starting point for the FOCUSS algorithm. The novelty of the FOCUSS algorithm comes from the fact that the weighting matrix $\mathbf{W}$ can be continuously updated using the previous solution. More specifically, suppose the $(l-1)$-th iteration of the image estimate is given by

$$\mathbf{x}_{l-1} = [x_{l-1;1}, x_{l-1;2}, \ldots, x_{l-1;N}]^T.$$

Then, the lth iteration of FOCUSS is composed of the following steps:

$$\text{Step 1:} \quad \mathbf{W}_l = \begin{pmatrix} |x_{l-1;1}|^p & 0 & \cdots & 0 \\ 0 & |x_{l-1;2}|^p & \cdots & 0 \\ \vdots & \vdots & \ddots & \vdots \\ 0 & 0 & \cdots & |x_{l-1;N}|^p \end{pmatrix}, \qquad [8]$$

$$\text{Step 2:} \quad \mathbf{q}_l = (\mathbf{A}\mathbf{W}_l)^\dagger \mathbf{y}, \qquad [9]$$

$$\text{Step 3:} \quad \mathbf{x}_l = \mathbf{W}_l \mathbf{q}_l, \qquad [10]$$

where the parameter p is given by $1/2 \le p \le 1$ (16). After $\mathbf{x}_l$ is obtained in Step 3, the weighting matrix is recalculated, and FOCUSS iteration, Step 1 to Step 3, is reapplied.

To understand why FOCUSS provides a sparse solution, consider the lth FOCUSS update. Using $\mathbf{q}_l = \mathbf{W}_l^{-1}\mathbf{x}_l$ with Eqs. [5] and [6], the lth FOCUSS update can be written by

$$\min \|\mathbf{W}_l^{-1}\mathbf{x}\|_2^2, \quad \text{s.t. } \mathbf{A}\mathbf{x} = \mathbf{y}. \qquad [11]$$

Suppose we set $p = 0.5$ for the $\mathbf{W}_l$ update. Then, we have the following asymptotic relation:

$$\begin{aligned}\|\mathbf{W}_l^{-1}\mathbf{x}\|_2^2 &= \mathbf{x}^T\left(\mathbf{W}_l^{-1}\right)^H\mathbf{W}_l^{-1}\mathbf{x} \\ &= \mathbf{x}^T\begin{pmatrix} |x_{l-1;1}|^{-1} & 0 & \cdots & 0 \\ 0 & |x_{l-1;2}|^{-1} & \cdots & 0 \\ \vdots & \vdots & \ddots & \vdots \\ 0 & 0 & \cdots & |x_{l-1;N}|^{-1} \end{pmatrix}\mathbf{x} \\ &\sim \sum_{i=1}^{N} |x_{l-1,i}| \\ &\sim \|\mathbf{x}\|_1 \ \text{ as } l \to \infty, \end{aligned} \qquad [12]$$

where the superscript ^{H} denotes the Hermitian transpose, and $\sim$ implies the asymptotic equality as $l \to \infty$. This implies that FOCUSS is asymptotically equivalent to the L_1 minimization problem. Since it is well known that L_1 minimization provides a sparse solution (12,13), we can expect that FOCUSS solution will be sparse.[1] The convergence of FOCUSS to a sparse solution was shown rigorously in a previous paper (15).

Note that FOCUSS starts by finding a low-resolution estimate of the sparse signal to initialize the $\mathbf{W}_l$ matrix at the beginning of an iteration, and this solution is pruned to a sparse signal representation. The pruning process is implemented by scaling the entries of the current solution by those of the solutions of previous iterations (15). Therefore, a good initial estimate is an important factor to guarantee the performance of the algorithm. As will be shown in the next section, projection reconstruction MR imaging provides a good initial estimate for FOCUSS. Therefore, we chose FOCUSS for an undersampled projection reconstruction MRI.

FOCUSS FOR PROJECTION RECONSTRUCTION

Let $f(\mathbf{r}), \mathbf{r} = (x, y) \in \Re^2$ denote the unknown proton density in 2D. Then, the k-space measurement from radial trajectory is given by

$$y(\mathbf{k}) = y(k,\theta) = \int f(\mathbf{r})e^{-j2\pi\mathbf{k}\cdot\mathbf{r}}d\mathbf{r}, \qquad [13]$$

where $\mathbf{k} = (k\cos\theta, k\sin\theta)$ denotes the coordinate vector in k-space, in which k-space samples are acquired according to the polar coordinate (k,θ), and $\mathbf{r} = (x, y)$ is the coordinate vector in spatial domain. Since the frequency encoding along the radial direction can be done simultaneously within a single echo, the resolution along the radial direction is assumed as the maximum. Hence, the total acquisition time is limited by the number of angular samples. At this point, the reconstruction problem is to obtain $f(\mathbf{r})$ from the k-space samples using Eq. [13]. Note that in radial acquisition, k-space samples are denser at the k-space center. The densely sampled k-space samples provide an image with acceptably low resolution, which is essential for the convergence of FOCUSS.

Recall that the well-known Fourier slice theory (19) tells us that Eq. [13] is indeed the Fourier transform of the following Radon transform with respect to s:

$$y(s,\theta) = \int f(x,y)\delta(x\cos\theta + y\sin\theta - s)dxdy, \qquad [14]$$

where $y(s,\theta)$ is obtained using the inverse Fourier transform of the k-space samples $y(k,\theta)$ along the radial direction. Now the reconstruction of $f(x,y)$ can be done using either the inverse Radon transform or filtered backprojection.

For the specific implementation of FOCUSS for projection reconstruction, we prefer a Radon space based reconstruction method to the k-space based Fourier gridding method. Historically, Fourier gridding methods using Eq. [13] have been more often used, since the cartesian grid allows the use of fast Fourier transform and fast inverse Fourier transform. However, gridding can add aliasing artifacts from the rectilinear resampling. Because of the recent advances of fast projection and backprojection algorithms (17,18), projection/backprojection using Eq. [14] is now becoming favorable over the gridding approaches. Hence, we will use the projection/backprojection approach.

For a computer implementation of projection/backprojection, the image domain should first be discretized into N pixels. Then, we may represent $f(x,y)$ as a sum of N basis functions $\{w_i(x,y)\}_{i=1}^N$ with weighting $f_i, i = 1,\ldots,N$:

$$f(x,y) = \sum_{i=1}^{N} f_i w_i(x,y), \qquad [15]$$

where $w_i(x,y)$ is 1 inside of the ith pixel and zero outside. The sinogram $y(s,\theta)$ in Eq. [14] is also discretized, and the jth projection ray can be represented by $y_j = y(s_j,\theta_j)$. Then, the Radon transform relation in Eq. [14] can be written as

$$\mathbf{y} = \mathbf{A}\mathbf{x}, \qquad [16]$$

where $\mathbf{y}$ and $\mathbf{x}$ may be represented by

$$\mathbf{y} = [y_1 \quad y_2 \quad \cdots \quad y_k]^T \in \mathbb{C}^K \qquad [17]$$

$$\mathbf{x} = [f_1 \quad f_2 \quad \cdots \quad f_N]^T \in \mathbb{C}^N \qquad [18]$$

and $\mathbf{A}$ is the $K \times N$ sparse matrix whose (j,i) elements can be calculated by

$$A_{j,i} = \int w_i(x,y)\delta(x\cos\theta_j + y\sin\theta_j - s_j)dxdy. \qquad [19]$$

Now, we are interested in reconstructing image $\mathbf{x}$ from very sparse, angularly sampled Radon space data, $\mathbf{y}$. To reduce

[1] Even for $P \ge 0.5$, FOCUSS still guarantees a sparse solution (15). However, throughout the article we use $P = 0.5$ for simplicity.

Table 1
Pseudo-code Implementation of PR-FOCUSS Using Fletcher-Reeves Conjugate Gradient Inner Loop

1. Initialize $\mathbf{x}_0 = \mathbf{A}^H\mathbf{y}$.
2. For each $l = 1, 2\ldots$, do the following:
   (a) Update $\mathbf{W}_l$ using Eq. [8].
   (b) Initialization for CG loop:

$$\mathbf{q}_l^{(0)} = \mathbf{O}, \quad \mathbf{g}^{(0)} = -\mathbf{W}_l^H\mathbf{A}^H\mathbf{y}, \quad \mathbf{d}^{(0)} = -\mathbf{g}^{(0)}.$$

   (c) Repeat the following CG steps until converged.
      (i) Compute the step size:

$$\alpha_n = -\frac{\mathbf{g}^{(n)H}\mathbf{d}^{(n)}}{\mathbf{d}^{(n)H}\mathbf{W}_l^H\mathbf{A}^H\mathbf{A}\mathbf{W}_l\mathbf{d}^{(n)}}.$$

      (ii) $\mathbf{q}_l^{(n+1)} = \mathbf{q}_l^{(n)} + \alpha_n\mathbf{d}^{(n)}$.
      (iii) $\mathbf{g}^{(n+1)} = -\mathbf{W}_l^H\mathbf{A}^H\left(\mathbf{y} - \mathbf{A}\mathbf{W}_l\mathbf{q}_l^{(n+1)}\right)$. If $\mathbf{g}^{(n+1)} = \mathbf{O}$, stop.
      (iv) Compute the following parameter:

$$\beta_n = \frac{\mathbf{g}^{(n+1)H}\mathbf{g}^{(n+1)}}{\mathbf{g}^{(n)H}\mathbf{g}^{(n)}}.$$

      (v) $\mathbf{d}^{(n+1)} = -\mathbf{g}^{(n+1)} + \beta_n\mathbf{d}^{(n)}$.
      (vi) Increase n and go to step (i).
   (d) $\mathbf{x}_l = \mathbf{W}_l\mathbf{q}_l^{(n+1)}$.
   (e) If converged stop. Otherwise, increase l and go to (a).

both angular sampling and angular aliasing artifacts, while maintaining spatial resolution, we employ FOCUSS, as described in Eqs. [8]–[10].

Note that the main computational burden for FOCUSS comes from the following pseudo-inverse calculation:

$$\mathbf{q}_l = (\mathbf{A}\mathbf{W}_l)^{\dagger}\mathbf{y} = \mathbf{W}_l^H\mathbf{A}^H\left(\mathbf{A}\mathbf{W}_l\mathbf{W}_l^H\mathbf{A}^H\right)^{-1}\mathbf{y}, \qquad [20]$$

because of the computationally expensive inversion of the $K \times K$ matrix $\mathbf{A}\mathbf{W}_l\mathbf{W}_l^H\mathbf{A}^H$. Here, the matrix inversion can be avoided by using the conjugate gradient (CG) method (20). The overall pseudo-code implementation of FOCUSS for projection reconstruction using CG is given in Table 1. As shown in Table 1, the main building block for CG is the calculation of the gradient:

$$\mathbf{g}^{(n+1)} = -\mathbf{W}_l^H\mathbf{A}^H\left(\mathbf{y} - \mathbf{A}\mathbf{W}_l\mathbf{q}_l^{(n+1)}\right). \qquad [21]$$

Note that, since the back-projection operation is adjoint of the projection operator (19), Eq. [21] can be decomposed into the following successive steps:

$$\text{Weighting:} \quad \mathbf{W}_l\mathbf{q}_l^{(n+1)}, \qquad [22]$$

$$\text{Projection:} \quad \mathbf{A}\mathbf{W}_l\mathbf{q}_l^{(n+1)}, \qquad [23]$$

$$\text{Substraction:} \quad \mathbf{y} - \mathbf{A}\mathbf{W}_l\mathbf{q}_l^{(n+1)}, \qquad [24]$$

$$\text{Backprojection:} \quad \mathbf{A}^H\left(\mathbf{y} - \mathbf{A}\mathbf{W}_l\mathbf{q}_l^{(n+1)}\right), \qquad [25]$$

$$\text{Weighting:} \quad -\mathbf{W}_l^H\mathbf{A}^H\left(\mathbf{y} - \mathbf{A}\mathbf{W}_l\mathbf{q}_l^{(n+1)}\right). \qquad [26]$$

The main computational burden comes from the projection operation, Eq. [23], and back-projection operation, Eq. [25]. However, the recent advances of fast projection and backprojection algorithms (17,18) may relieve the computational burden of these steps significantly.

FIG. 1. Original Shepp-Logan phantom image.

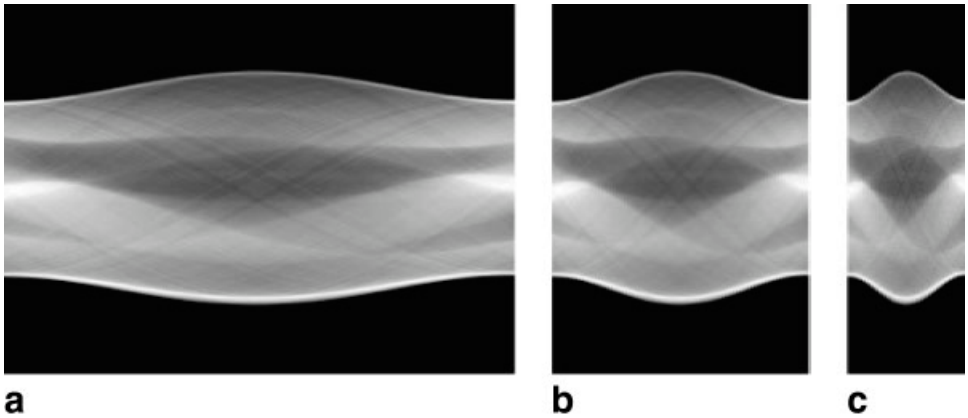

FIG. 2. Sinogram data from Shepp-Logan phantom. Projection data from (**a**) 180 views, (**b**) 90 views, and (**c**) 45 views, respectively.

EXPERIMENTAL RESULTS

Synthetic Data

To analyze the efficiency of our algorithm (PR-FOCUSS) in a controlled environment, extensive computer simulations were performed using the popular Shepp-Logan phantom, as shown in Fig. 1. For a fair evaluation of the performance of PR-FOCUSS, we also implemented three standard reconstruction methods: (a) filtered back-projection with linear interpolation and a Ram-Lak filter (LIN-FBP), (b) filtered back-projection with spline interpolation with a Ram-Lak filter (SPLINE-FBP), and (c) an iterative reconstruction method using the conjugate gradient method (CG-ALONE).

Recall that in the discrete implementation of back-projection, the ray passes through the center of the pixel to the detector cells; hence, the contribution of the detector measurements are calculated based on the interpolation from the adjacent detector measurements (19). Here, LIN-FBP uses linear interpolation, whereas SPLINE-FBP uses spline based interpolation. The reason for including SPLINE-FBP is to check whether higher order interpolation might improve the reconstruction quality.

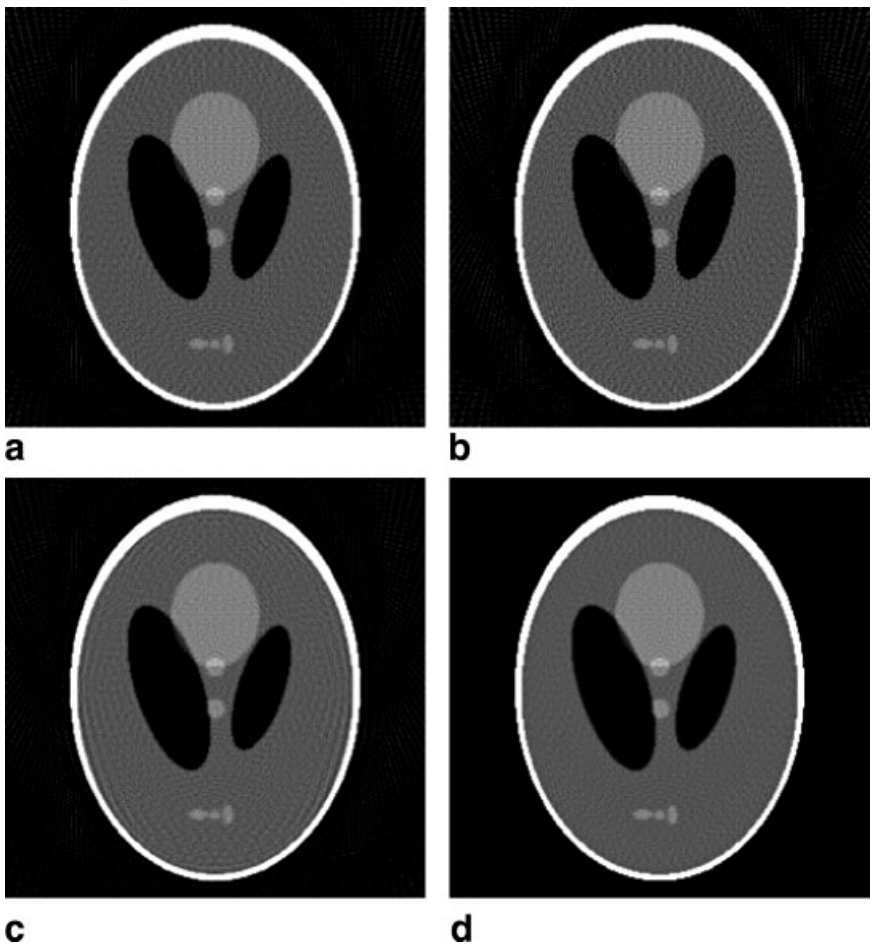

FIG. 3. Reconstruction results from 90 views using (**a**) the filtered back projection algorithm (linear interpolation, Ram-Lak filter), (**b**) the filtered back projection algorithm (spline interpolation, Ram-Lak filter), (**c**) the conjugate gradient method, and (**d**) PR-FOCUSS.

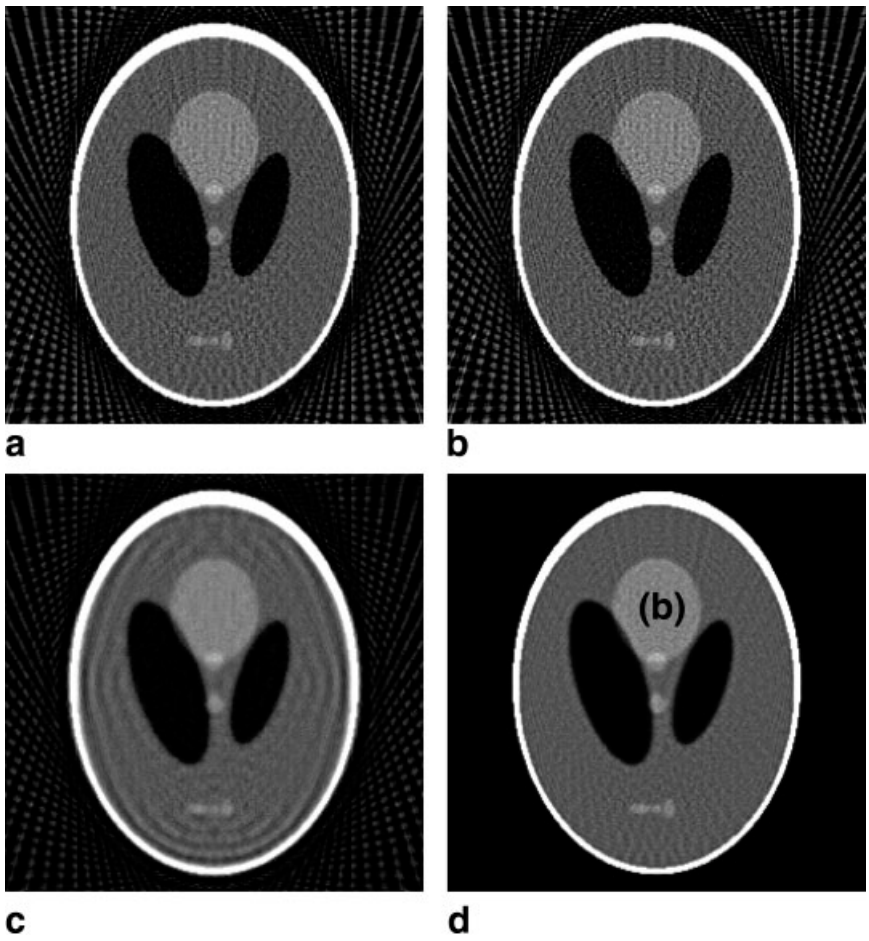

FIG. 4. Reconstruction results from 45 views using (**a**) the filtered back projection algorithm (linear interpolation, Ram-Lak filter), (**b**) the filtered back projection algorithm (spline interpolation, Ram-Lak filter), (**c**) the conjugate gradient method, and (**d**) PR-FOCUSS.

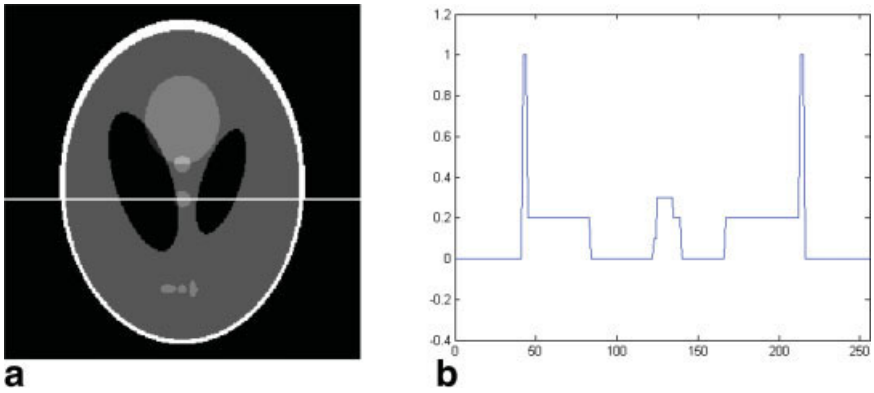

FIG. 5. (**a**) Position for the cutview inspection, and (**b**) intensity profile along the cutview of the original image. [Color figure can be viewed in the online issue, which is available at www.interscience.wiley.com.]

The CG-ALONE method is an iterative implementation to obtain the minimum norm solution by minimizing the constrained minimization problem in Eq. [3]. Since the conjugate gradient method is known to provide stable reconstruction and has been employed in projection reconstruction MRI with multiple coils (21), we want to know whether CG-ALONE can eliminate the undersampling artifacts. Note that the main difference between CG-ALONE and PR-FOCUSS is that the weighting matrix $\mathbf{W}_l$ is not updated in CG-ALONE. Other than that, the two algorithms are very similar, and PR-FOCUSS also employs the CG iteration for each updated $\mathbf{W}_l$. For a fair comparison between CG-ALONE and PR-FOCUSS, 100 iterations were used in CG-ALONE, whereas PR-FOCUSS updated $\mathbf{W}_l$ 20 times, with 5 CG inner iterations for each updated $\mathbf{W}_l$. Hence, the total number of iterations in PR-FOCUSS was $20 \times 5 = 100$, which is identical to that of CG-ALONE. The reason for applying so many iterations was to show that we are not artificially limiting the number of PR-FOCUSS iterations; rather, we want to demonstrate that the reconstruction error continues to decrease for additional iterations.[2] All the standard algorithms, as well as PR-FOCUSS, were implemented using MATLAB (Mathworks, Natick, MA).

[2]Usually, however, a much smaller number of FOCUSS iterations was sufficient for most of the simulation environments.

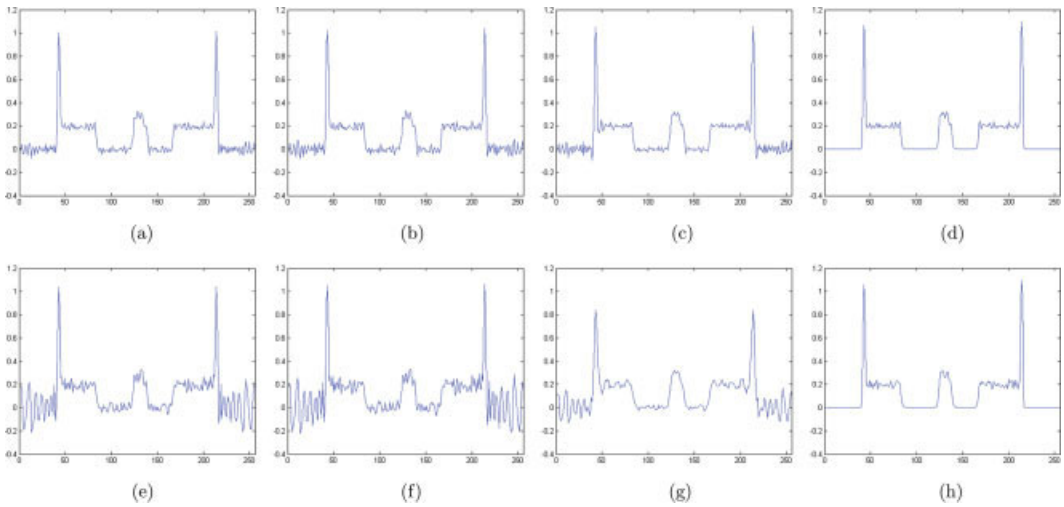

FIG. 6. Top: Intensity profile along the cutview for an image reconstructed from 90 views using (**a**) the filtered back projection algorithm (linear interpolation, Ram-Lak filter), (**b**) the filtered back projection algorithm (spline interpolation, Ram-Lak filter), (**c**) the conjugate gradient method, and (**d**) PR-FOCUSS. Bottom: Intensity profile along the cutview for image reconstructed from 45 views using (**e**) the filtered back projection algorithm (linear interpolation, Ram-Lak filter), (**f**) the filtered back projection algorithm (spline interpolation, Ram-Lak filter), (**g**) the conjugate gradient method, and (**h**) PR-FOCUSS. [Color figure can be viewed in the online issue, which is available at www.interscience.wiley.com.]

In this simulation, we collected data from 0 to 179 degrees, which is similar to the half-scan in X-ray computed tomography (X-ray CT). Full angle sinogram data with 180 projection views were generated from the phantom using the Radon transform, as shown in Fig. 2a, and an angular down-sampling operation was performed to obtain 90 projection views and 45 projection views, as shown in Figs. 2b and 2c, respectively.

Figures 3a–3d show the reconstruction results from 90 views using LIN-FBP, SPLINE-FBP, CG-ALONE, and the proposed PR-FOCUSS, respectively. The image scale window is modified to saturate the skull so that the artifacts are more obvious. The modified image scale window is consistent for all four reconstructions. We can observe that the view-related aliasing artifacts mostly disappeared in the PR-FOCUSS reconstruction results,

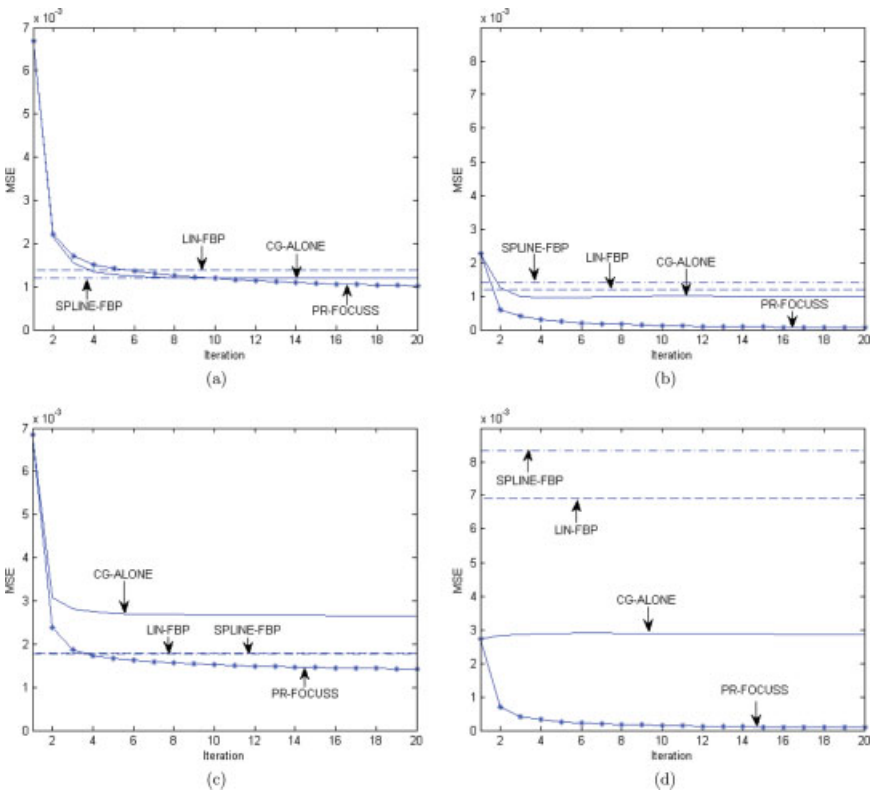

FIG. 7. Top: MSE error plots for (**a**) inside and (**b**) outside of the objects in the reconstruction images from 90 views. Bottom: MSE plots for (**c**) inside and (**d**) outside of the objects in the reconstructed images from 45 views. [Color figure can be viewed in the online issue, which is available at www.interscience.wiley.com.]

while the sharpness of the original image was maintained. Figures 4a–4d show the reconstruction results from 45 views using LIN-FBP, SPLINE-FBP, CG-ALONE, and the proposed PR-FOCUSS, respectively. Again, the image scale is consistently modified to saturate the skull so that the artifacts are more obvious. Most of the aliasing artifacts observed in the conventional LIN-FBP, SPLINE-FBP, and CG-ALONE were suppressed in the reconstruction results by PR-FOCUSS. As the number of views decreases, many severe view aliasing artifacts and much resolution loss were observed in the reconstruction results by LIN-FBP, SPLINE-FBP, and CG-ALONE. However, only slight degradation of image quality was observed in the PR-FOCUSS results.

To demonstrate the improved performance of the proposed PR-FOCUSS more clearly, the intensity profiles along a cutview of images from 90 views and 45 views are plotted. Figures 5a and 5b show the position of the cutview and the intensity profile, respectively. Figures 6a–6h clearly show that PR-FOCUSS retains the contrast of the original phantom and removes the aliasing artifacts in the background.

To quantify the quality improvement of PR-FOCUSS, we have calculated the mean square errors (MSE) and have plotted them according to the iteration number (see Figs. 7a–7d). The MSE of the lth PR-FOCUSS reconstruction $\mathbf{x}_l$ is defined by

$$\text{MSE} = \frac{\|\mathbf{x}_l - \mathbf{x}_{\text{org}}\|_2^2}{\|\mathbf{x}_{\text{org}}\|_2^2}, \qquad [27]$$

where $\|\cdot\|_2$ denotes the L_2 norm and $\mathbf{x}_{\text{org}}$ is the original image. Since one iteration of PR-FOCUSS corresponds to five CG-ALONE iterations, for a fair comparison, we also consider five CG iterations in a CG-ALONE algorithm as one CG-ALONE iteration. Therefore, even though the maximum number of iterations in Figs. 7a–7d reads 20, it corresponds to 100 CG iterations. The MSE of the lth CG-ALONE iteration is also calculated similar to Eq. [27]. Since the LIN-FBP and SPLINE-FBP are not iterative algorithms, the MSE is consistent regardless of iteration number. Figures 7a and 7c show that the MSE of the foreground objects reconstructed by PR-FOCUSS for both 90 and 45 views is smallest among all the methods and is continuously reduced with each iteration. Also, note that the MSE of CG-ALONE is saturated and is not improved with further iterations. A similar trend can be observed in the background region, as shown in Figs. 7b and 7d. The MSE of PR-FOCUSS is significantly lower than those of the other methods, and it nearly reaches zero as iterations continue.

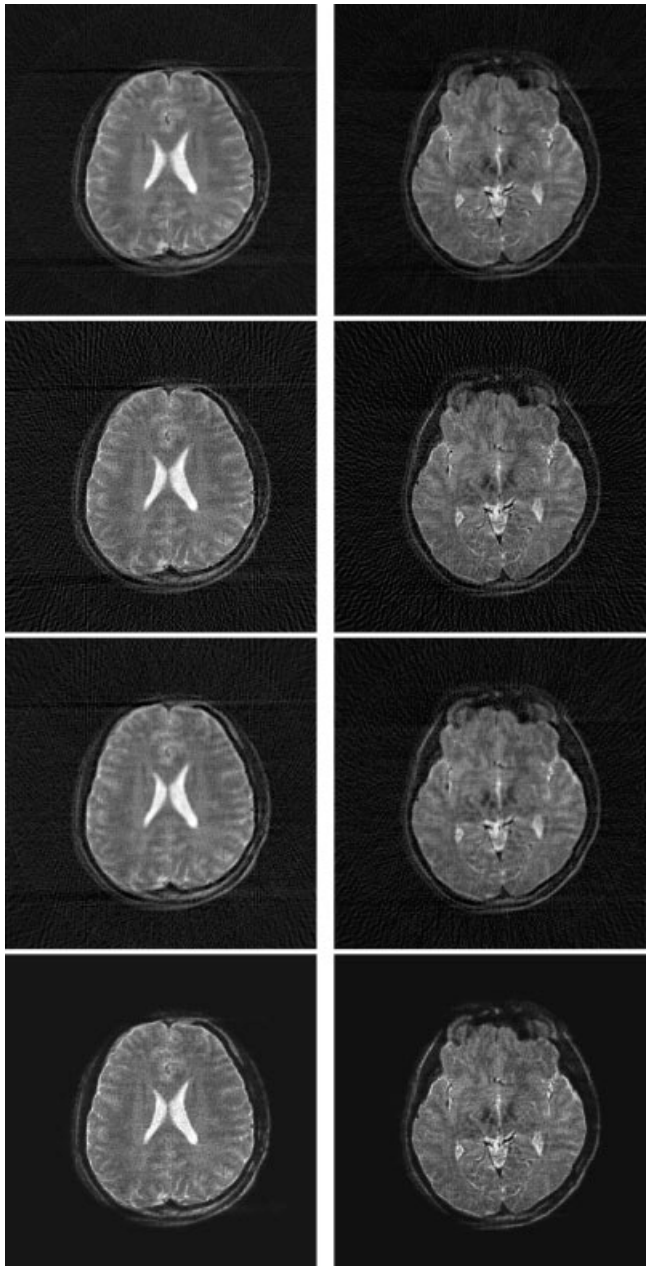

FIG. 8. Reconstruction results from a half-scan with uniform angular sampling between $0^\circ - 180^\circ$. 1st row: Reference reconstruction from 180 views. 2nd row: Reconstruction results from 90 views using LIN-FBP. 3rd row: Reconstruction results from 90 views using CG-ALONE. 4th row: Reconstruction results from 90 views using PR-FOCUSS.

In Vivo Experiments

To evaluate the practical usefulness of PR-FOCUSS, we apply the PR-FOCUSS algorithm to in vivo brain data. In this work, two healthy volunteers participated. Informed consent was obtained from each volunteer. In vivo brain data were acquired with the radial spin-echo sequence using a 3.0T MRI system manufactured by ISOL technology of Korea. A birdcage RF head coil was used for both the RF pulse transmission and the signal detection. The images were acquired with a slice thickness of 4 mm using TR/TE=2000/90 ms. 256 points per projection were acquired with an FOV of 220×220 mm^2 to produce images with 256×256 resolution. Twenty slices were acquired with a slice thickness of 4 mm. Three separate scans were performed for each subject to acquire 180 views, 90 views, and 45 views, respectively. To show the robustness of PR-FOCUSS, we have applied PR-FOCUSS for different slices of a brain. In addition, for fair comparison with the standard methods, the reconstruction results from the conventional

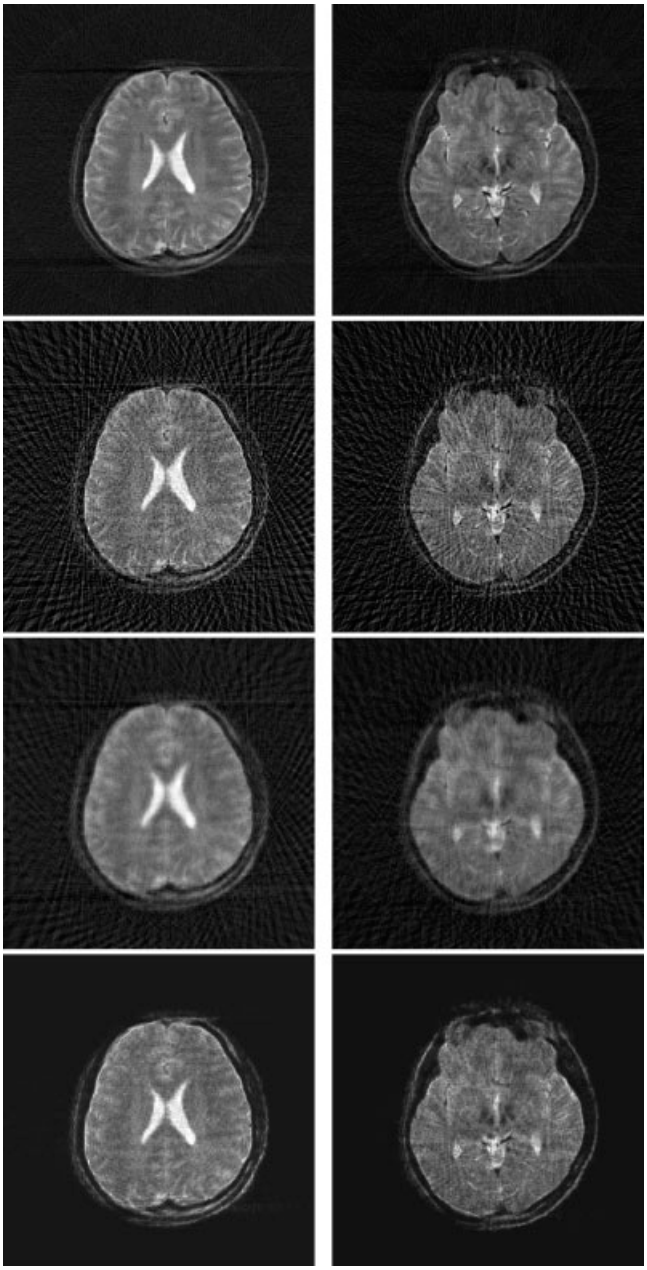

FIG. 9. Reconstruction results from half-scan with uniform angular sampling between 0°–180°. 1st row: Reference reconstruction from 180 views. 2nd row: Reconstruction results from 45 views using LIN-FBP. 3rd row: Reconstruction results from 45 views using CG-ALONE. 4th row: Reconstruction results from 45 views using PR-FOCUSS.

back projection (LIN-FBP)[3] and conjugate gradient method (CG-ALONE) are also generated. Furthermore, we generated the reconstruction results using the full 180 views as references. Since the 180 views were obtained from a separate experiment, there might be registration errors in the reconstructions; however, they still provide useful ground-truth images.

[3]Since LIN-FBP performs similarly to SPLINE-FBP, as shown in Fig. 7, we have omitted the results by SPLINE-FBP to save space.

Figure 8 shows the reconstruction results using various algorithms for the 90 view projection data. The second, the third, and the fourth rows of Fig. 8 correspond to reconstructed images using LIN-FBP, CG-ALONE, and PR-FOCUSS, respectively. PR-FOCUSS results are superior to those of the other methods. Furthermore, the PR-FOCUSS results are comparable to the reconstruction from the full 180 view projections shown in the first row of Fig. 8. We also compared our algorithm with the other methods for the case of 45 view projections (see Fig. 9). Again,

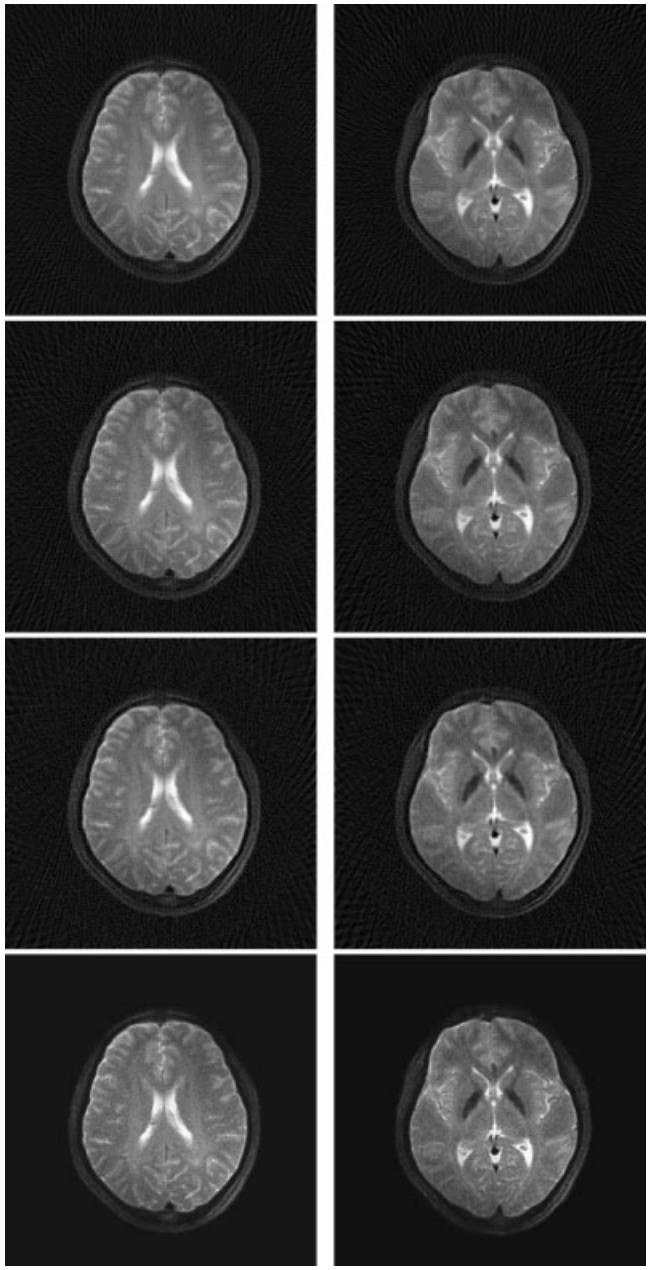

FIG. 10. Reconstruction results from full-scan with uniform angular sampling between 0°–360°. 1st row: Reference reconstruction from 190 views. 2nd row: Reconstruction results from 103 views using LIN-FBP. 3rd row: Reconstruction results from 103 views using CG-ALONE. 4th row: Reconstruction results from 103 views using PR-FOCUSS.

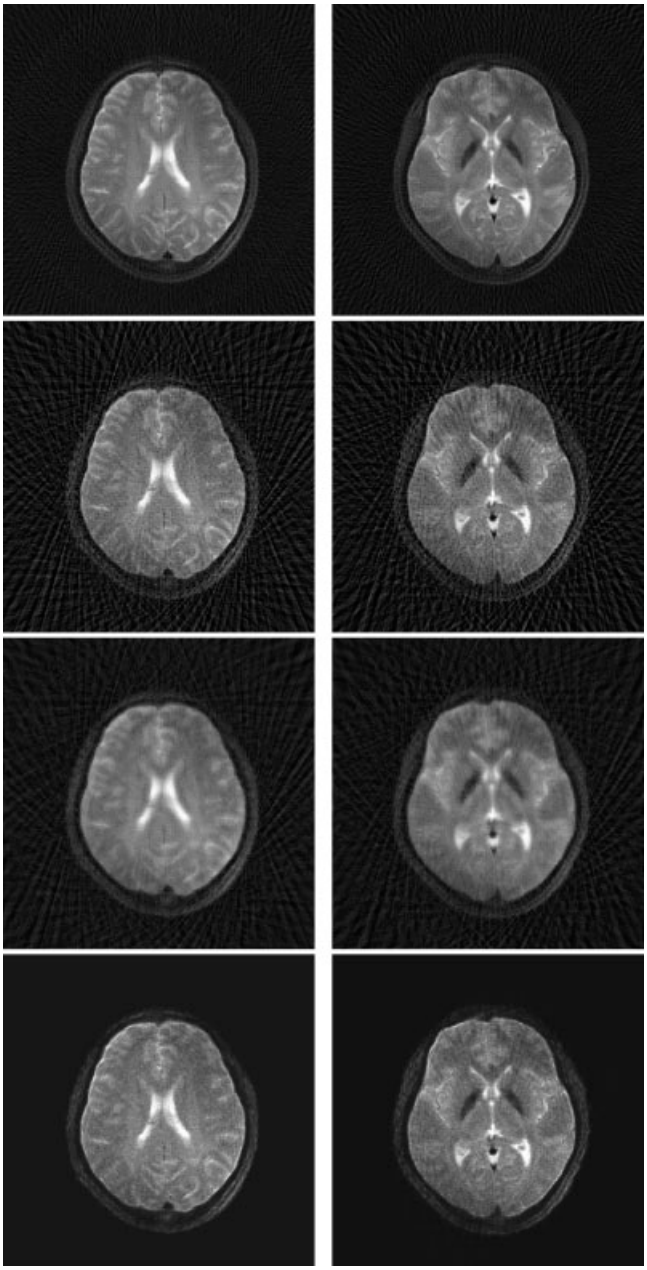

FIG. 11. Reconstruction results from full-scan with uniform angular sampling between 0°–360°. 1st row: Reference reconstruction from 190 views. 2nd row: Reconstruction results from 51 views using LIN-FBP. 3rd row: Reconstruction results from 51 views using CG-ALONE. 4th row: Reconstruction results from 51 views using PR-FOCUSS.

the reconstructed images using PR-FOCUSS show quality improvements over the conventional methods.

Note that the horizontal streaks from the top and the bottom of all the scans in Figs. 8 and 9 are due to a timing error. A delay caused the 0 and 179 degree projections to be shifted, which produced these streaks.[4] To eliminate these artifacts, we performed another scan with uniformly sampled views between 0° and 360°, which corresponded to a full-scan in X-ray CT. More specifically, three separate scans were performed for each subject to acquire 190 views, 103 views, and 51 views, respectively. Hence, the corresponding view step sizes were 360/190°, 360/103°, and 360/51°, respectively. The reconstruction results from the reference scan using 190 views and the view downsampled reconstruction results using LIN-FBP, CG-ALONE, and PR-FOCUSS with 103 views are illustrated in the first, the second, the third and the fourth rows of Fig. 10, respectively. PR-FOCUSS reconstruction performed better than the conventional methods, especially at the background, and the object reconstruction image quality was comparable for all three methods. Similar results can be observed from reconstruction results from 51 views, as shown in Fig. 11. The PR-FOCUSS reconstructions are consistently better than the conventional algorithms.

DISCUSSION

Sparsity

The basis for our algorithm is the sparsity of image support. Formally, the sparsity is defined by the number of nonzero pixels in an image domain (12,13). Then, one may wonder (a) when are images not sparse enough for our algorithm to work and (b) are there any graceful degradations or severe artifacts when the images are not sparse?

The main theoretical framework to answer these questions is the recent theory of *compressed sensing* (12,13) in the signal processing community. The compressed sensing theory tells us that the *perfect* reconstruction of $\mathbf{x}$ is possible from the *noiseless* k-space measurements markedly smaller than the Nyquist sampling limit as long as the nonzero support of $\mathbf{x}$ is sparse and the k-space samples are obtained in random or radial sampling patterns (12,13). More specifically, suppose the N dimensional vector $\mathbf{x}$ is nonzero at the *unknown* $M(\ll N)$ locations, and the dimension of the k-space measurement vector $\mathbf{y}$ is K. Then, it is possible to design $K = O(M \log N)$ number of k-space measurements to obtain the perfect reconstruction of $\mathbf{x}$ with overwhelming probability.[5] Second, if $K = O(M \log^6 N)$ discrete measurements in k-space are *noisy* and their magnitudes are upper-bounded by the input noise power ϵ, then with overwhelming probability the reconstruction error is also upper bounded by ϵ multiplied with a finite constant. This implies that, unlike the common belief that the ill-posed problem is *unstable*, the sparsity of the unknown image makes the reconstruction process *stable*. Third, if the signal $\mathbf{x}$ is compressible in the sense that the reordered entries $x_{(n)}$ decay like a power-law,

$$|x_{(n)}| \leq C \cdot n^{-1/q},$$

for a positive constant C and $0 < q < 1$, where $x_{(n)}$ denotes the nth largest $\mathbf{x}$ values in a discrete domain, then with

[4]The authors would like to thank the anonymous reviewer for bringing this issue to our attention. This paragraph was quoted from the reviewer's comment.

[5]The $O(\cdot)$ denotes the "big O" notation to describe an asymptotic upper bound.

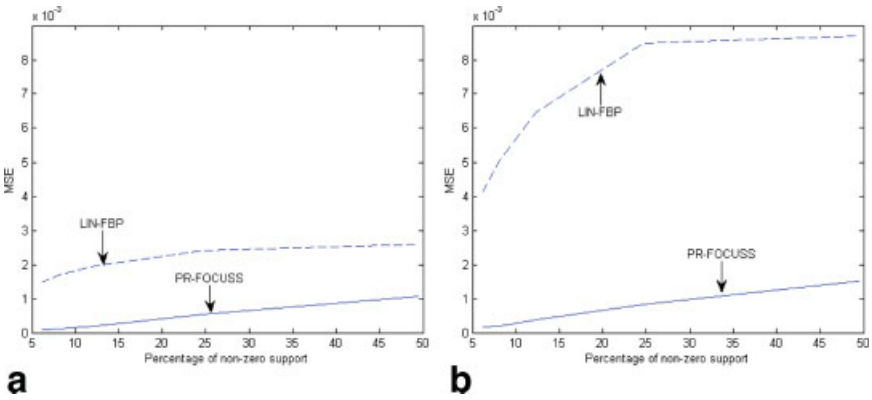

FIG. 12. MSE plots of LIN-FBP and PR-FOCUSS with respect to the percentage of non-zero support. MSE plots from (**a**) 90 views and (**b**) 45 views.

overwhelming probability one can reconstruct the signal $\mathbf{x}$ from K measurements with the reconstruction error

$$\|\mathbf{x} - \hat{\mathbf{x}}^K\|_2 \leq C_r \cdot (K/\log N)^{-(1/q-1/2)}, \qquad [28]$$

for some finite constant C_r, where $\hat{\mathbf{x}}^K$ denotes the estimate of $\mathbf{x}$ from K measurements (12,13). This is an especially useful result for MR imaging since, in many cases, the images are not sparse, but they are compressible in the sense that the magnitude of the $\mathbf{x}$ decays rapidly. Hence, Eq. [28] guarantees the *graceful degradation* of the reconstruction image quality even if the sparsity assumption breaks down.

Perhaps the most important implication of the compressed sensing theory is that the optimal sparse solution satisfying the above-mentioned properties can be obtained by solving the L_1 minimization (12,13). More specifically, the optimal MR imaging problem from the compressed sensing perspective can be stated as follows:

$$\begin{aligned} &\text{minimize } \|\mathbf{x}\|_1, \\ &\text{subject to } \mathbf{y} = \mathbf{A}\mathbf{x}, \end{aligned} \qquad [29]$$

where $\|\cdot\|_1$ denotes the L_1. Since our cost function, Eq. [11], is asymptotically equivalent to Eq. [29], we can expect that our algorithm is asymptotically optimal from a compressed sensing perspective. Thus, it inherits all of the above-mentioned desirable properties of the compressed sensing.

To demonstrate the graceful degradation of our algorithm when the sparsity assumption breaks down, we have generated a series of Shepp-Logan phantoms of varying object size with respect to the fixed image size of 256 × 256. The MSE errors of our algorithm from 90 views and 45 views with respect to the percentage of nonzero support is illustrated in Figs. 12a and 12b, respectively. The linear increase of the MSE of our algorithm with respect to the nonzero supports implies the graceful degradation of image quality as the support size increases. However, for the case of LIN-FBP, the MSE increases abruptly and it is soon saturated.

Noisy Measurement

The basic assumption of the derivation of our algorithm is that the signal to noise ratio (SNR) of a k-space measurement is reasonably high, since the forward model is given by Eq. [2]. This is typical of a modern MRI scanner due to the advance of MR hardware. However, depending on the acquisition protocols, there might be cases where the SNR is not sufficient and the k-space data includes significant noise. In these cases, the forward model given in Eq. [2] should be modified as follows:

$$\mathbf{y} = \mathbf{A}\mathbf{x} + \mathbf{n}, \qquad [30]$$

where $\mathbf{n}$ denotes the noise. Therefore, the equality constraint in Eq. [6] should be changed to the following inequality constraint:

$$\min \|\mathbf{q}\|_2^2, \quad \text{s.t. } \|\mathbf{y} - \mathbf{A}\mathbf{W}_l\mathbf{q}\|_2 \leq \epsilon, \qquad [31]$$

where $\mathbf{W}_l$ denotes the lth weighting matrix, and ϵ is the noise level. The constrained optimization problem can be converted into an unconstrained optimization problem using the Lagrangian multiplier (20):

$$C(\mathbf{q}) = \|\mathbf{y} - \mathbf{A}\mathbf{W}_l\mathbf{q}\|_2^2 + \lambda\|\mathbf{q}\|_2^2, \qquad [32]$$

where λ denotes the appropriate Lagrangian parameter. Finally, the optimal lth update is then given by

$$\begin{aligned} \mathbf{x}_l &= \mathbf{W}_l\mathbf{q} \\ &= \mathbf{\Theta}_l\mathbf{A}^H\left(\mathbf{A}\mathbf{\Theta}_l\mathbf{A}^H + \lambda\mathbf{I}\right)^{-1}\mathbf{y}, \end{aligned} \qquad [33]$$

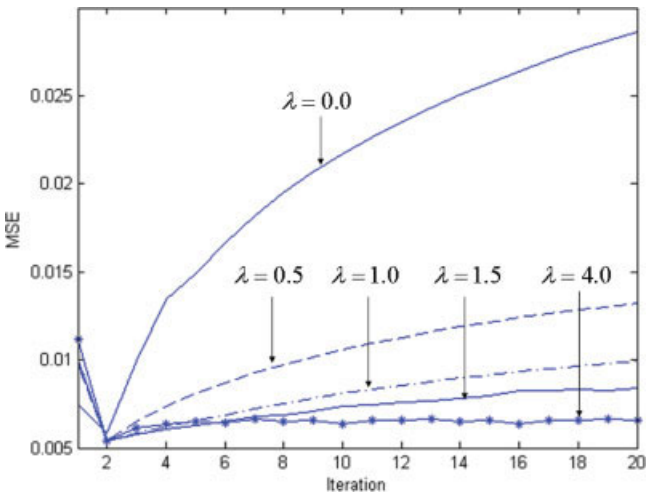

FIG. 13. MSE plots of PR-FOCUSS from noisy 45 views with respect to the regularization parameter λ.

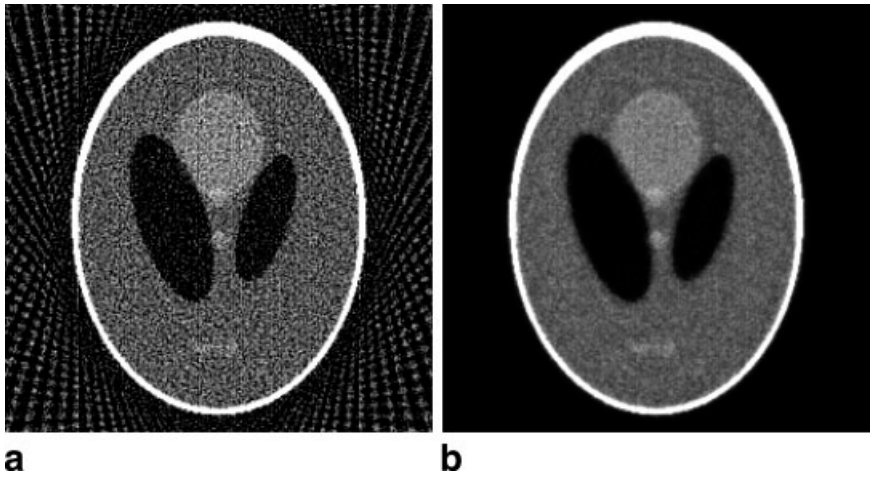

FIG. 14. Reconstruction results from noisy 45 views using (**a**) LIN-FBP and (**b**) regularized PR-FOCUSS.

where $\mathbf{\Theta}_l = \mathbf{W}_l \mathbf{W}_l^H$. To quantify the performance of our algorithm under a noisy scenario, we generate the noisy k-space measurement from Shepp-Logan phantoms by adding zero mean Gaussian noise to the sinogram data. Figure 13 illustrates the MSE error of our algorithm with different λ values. The original algorithm with $\lambda = 0$ diverges after several iterations, since it assumes noise free measurements. By increasing the λ values, the algorithm becomes more stable, and the solution becomes smoother, as shown in Fig. 14.

CONCLUSION

We proposed the projection reconstruction FOCUSS (PR-FOCUSS) algorithm to obtain a high resolution reconstruction from angularly undersampled radial k-space data. The FOCUSS algorithm was found to be suitable for projection reconstruction MRI, because such medical images are usually sparse, and the center area of the undersampled PR k-space samples still provides a low resolution, yet meaningful, image essential for the success of FOCUSS. A conjugate gradient method using projection/backprojection operation was developed to implement each step of PR-FOCUSS, whose computational burden could be significantly reduced by using the fast projection/back projection algorithms. Simulation results, as well as a real in vivo brain data set from a 3.0T MRI scanner, demonstrated that the proposed algorithm suppresses the angular aliasing artifacts with minimal resolution loss.

REFERENCES

1. Lauterbur PC. Image formation by induced local interactions; examples employing nuclear magnetic resonance. Nature 1973;242:190–191.
2. Glover GH, Pauly JM. Projection reconstruction techniques for reduction of motion effects in MRI. Magn Reson Med 1992;28:275–289.
3. Bernstein MA, King KF, Zhou XJ. Handbook of MRI pulse sequences. St. Louis, MO: Academic Press; 2004.
4. Ra JB, Hilal SK, Oh CH. An algorithm for MR imaging of the short T2 fraction of sodium using the FID signal. J Comput Assist Tomogr 1989;13:302–309.
5. Boada FE, Gillen JS, Shen GX, Chang SY, Thulborn KR. Fast three dimensional sodium imaging. Magn Reson Med 1997;37:706–715.
6. Jung KJ, Cho ZH. Reduction of motion artifacts in NMR diffusion imaging using view angle tilted line-integral projection reconstruction. Magn Reson Med 1991;19:349–360.
7. Gmitro AF, Alexander AL. Use of a projection reconstruction method to decrease motion sensitivity in diffusion-weighted MRI. Magn Reson Med 1993;29:835–838.
8. Peters Dana C, Korosec Frank R, Grist Thomas M, Block Walter F, Holden James E, Vigen Karl K, Mistretta Charles A. Undersampled projection reconstruction applied to MR angiography. Magn Reson Med 2000;43:91–101.
9. Lustig M, Santos JM, Donoho DL, Pauly JM. k-t SPARSE: High frame rate dynamic MRI exploiting spatio-temporal sparsity. In: Proceedings of ISMRM, Seattle, WA, 2006.
10. Lustig M, Donoho DL, Pauly JM. Rapid MR imaging with compressed sensing and randomly under-sampled 3DFT trajectories. In: Proceedings of ISMRM, Seattle, WA, 2006.
11. Mistretta CA, Wieben O, Velikina J, Block W, Perry J, Wu Y, Johnson K, Wu Y. Highly constrained backprojection for time-resolved MRI. Magn Reson Med 2006;55:30–40.
12. Donoho DL. Compressed sensing. IEEE Trans on Information Theory 2006;52:1289–1306.
13. Emmanuel Candes, Justin Romberg, Terence Tao. Robust uncertainty principles: Exact signal reconstruction from highly incomplete frequency information. IEEE Trans on Information Theory 2006;52:489–506.
14. Gorodnitsky IF, George JS, Rao BD. Neuromagnetic source imaging with FOCUSS: a recursive weighted minimum norm algorithm. Electroencephalogr Clin Neurophysiol 1995;95:231–251.
15. Gorodnitsky IF, Rao BD. Sparse signal reconstruction from limited data using FOCUSS: re-weighted minimum norm algorithm. IEEE Trans on Signal Processing 1997;45:600–616.
16. Kreutz-Delgado K, Murray JF, Rao BD, Engan K, Lee TW, Sejnowski TJ. Dictionary learning algorithms for sparse representation. Neural Computation 2003;15:349–396.
17. Samit Basu, Yoram Bresler. $O(N^2 \log_2 N)$ filtered backprojection reconstruction algorithm for tomography. IEEE Trans on Image Processing 2000;9:1760–1773.
18. Fessler J, Sutton BP. Nonuniform fast Fourier transforms using min-max interpolation. IEEE Trans on Signal Processing 2003;2:560–574.
19. Kak AC, Slaney M, Principles of computerized tomographic imaging. Philadelphia: SIAM Press; 2001.
20. Chong EKP, Zak SH. An introduction to optimization. New York: Wiley-Interscience; 1996.
21. Pruessmann KP, Weiger M, Bornert P, Boesiger P. Advances in sensitivity encoding with arbitrary k-space trajectories. Magn Reson Med 2001;46:638–651.